ADVANCED FUNCTIONAL MATERIALS
www.afm-journal.de

Thermal Conductivity Reduction in a Nanophononic Metamaterial versus a Nanophononic Crystal: A Review and Comparative Analysis

Mahmoud I. Hussein, Chia-Nien Tsai, and Hossein Honarvar*

The notion of a locally resonant metamaterial—widely applied to light and sound—has recently been introduced to heat, whereby the thermal conductivity is reduced primarily by intrinsic localized atomic vibrations rather than scattering mechanisms. This article reviews and analyzes this new emerging concept, termed nanophononic metamaterial (NPM), and contrasts it with the competing concept of a nanophononic crystal (NPC) in which thermal conductivity reduction is realized primarily via nanoscale Bragg scattering. Both the NPM and NPC core mechanisms require the presence of a sufficient level of wave behavior, which is possible when there is a relatively wide distribution of the phonon mean free path (MFP). Silicon serves as a perfect material to form NPMs and NPCs given its relatively large average phonon MFP. This offers a unique opportunity considering silicon's abundance and mature fabrication technology. It is shown in this comparative study that while both the NPM and NPC nanosystems may be rendered to serve as extreme insulators of heat, an NPM may do so without excessive reduction in the minimum feature size–which is key to keeping the electrical properties intact. This trait makes a silicon-based NPM poised to serve as a low-cost thermoelectric material with exceptional performance.

1. Introduction

The lattice conduction of thermal energy in crystalline solids is a process that involves several atomic-scale phonon mechanisms with a complex interplay between wavelike motion and diffusive scattering.[1] In a material environment, a low-amplitude phonon mode—characterized by frequency, wave vector, and polarization—may in principle travel relatively long distances without scattering with other phonon modes. This is true despite their short wavelengths. When the amplitude is large, however, nonlinear effects supervene and phonons scatter among themselves. Phonons also scatter with non-pristine boundaries if present along their paths. The average distance a phonon travels before it scatters represents its mean free path (MFP). Since thermal transport is carried by a large population of phonons spanning a frequency spectrum (that typically covers several terahertz), the MFP exhibits a distribution whose mean is denoted the average MFP. As the temperature increases, the phonon amplitudes increase and the average MFP drops.

In conventional bulk sized materials, the average MFP is small compared to the sample size; thus the phonons seldom have the opportunity to travel all the way to the boundaries before losing their wave character. In such an environment, the phonons travel in a 3D medium with practically an indefinite extent, i.e., effectively a medium with infinitely sized dimensions. Under these conditions, only the wave dispersion characteristics pertaining to a primitive unit cell—which consists of only two atoms in silicon—are relevant to the underlying thermal transport mechanisms. In a nanostructured material on the other hand, the average MFP could span a distance on the order of, or larger than, the dimensions of the nanostructure. In this case, an additional set of wave dispersion characteristics contribute to the transport dynamics, and that is the phonon dispersion pertaining to the nanostructured unit cell (assuming periodicity). **Figure 1**a represents a "large" nanostructure of silicon that is effectively *bulk silicon* and Figure 1b represents a "small" counterpart that may be denoted *nano silicon*.

In this article, we provide a literature and technical review of an emerging type of nanostructure, nanophononic metamaterials (NPMs),[2,3] that has highly favorable properties to serve as a thermoelectric material for the conversion of heat to electricity and vice versa.[4] To place the performance of NPMs in perspective, we also consider another key class of nanostructures, nanophononic crystals (NPCs),[5,6] and provide

Prof. M. I. Hussein, C.-N. Tsai, Dr. H. Honarvar
Ann and H.J. Smead Department of Aerospace Engineering Sciences
University of Colorado Boulder
Boulder, CO 80303, USA
E-mail: mih@colorado.edu
Prof. M. I. Hussein, Dr. H. Honarvar
Department of Physics
University of Colorado Boulder
Boulder, CO 80309, USA
Dr. H. Honarvar
JILA
University of Colorado Boulder
Boulder, CO 80309, USA
The ORCID identification number(s) for the author(s) of this article can be found under https://doi.org/10.1002/adfm.201906718.

DOI: 10.1002/adfm.201906718

 © 2019 WILEY-VCH Verlag GmbH & Co. KGaA, Weinheim

a comparative analysis of their thermal transport properties. Both NPMs and NPCs exhibit their favorable properties from their internal nanostructure, each with a unique prime mechanism that is rooted in wave behavior. While in principle this allows for use of a wide range of constituent materials, both systems are optimal when realized from a constituent material that enjoys large phonon MFPs. Silicon has this advantage; it exhibits a phonon MFP distribution that ranges from a few nanometers to tens of microns at room temperature.[7] For this reason, we focus our investigation on silicon-based NPMs and NPCs.

2. Thermal Transport in Nanostructured Membranes

In the past two decades, nanostructuring has emerged as a powerful approach for manipulating phonon motion and realizing new material properties and device functions for several applications involving thermal management.[8–12] In this review, we focus mainly on a class of nanostructured material systems in which the geometry is extended indefinitely in the planar directions, and truncated at some finite thickness in the out-of-plane direction. We start with the most basic configuration in this class, a suspended uniform membrane, and go over a model for prediction of the in-plane thermal conductivity in this system. We then introduce NPCs and NPMs and review the literature on these systems in general and, more specifically, on membrane-based NPCs and NPMs. In the course of the section, we use the uniform membrane modeling framework as a foundation to treating thermal transport in membrane-based NPCs and NPMs.

2.1. Uniform Membrane

The lattice thermal conductivity of a crystal may be mechanistically elucidated by examining the Boltzmann transport equation (BTE) following the single-mode-relaxation time (SMRT) approximation.[1,13] For a membrane-like material with free surfaces at the top and the bottom, this equation is applied to the unit cell shown in **Figure 2**a and takes the form

$$k = \underbrace{\frac{1}{V}\frac{A_c}{4\pi}\sum_m \int_0^{\kappa_{max}} C(\kappa,m)v_g^2(\kappa,m)\tau(\kappa,m)\kappa d\kappa}_{K} \quad (1)$$

where A_c is the unit-cell cross-sectional area (i.e., area of dimensions $aA_x \times aA_y$, where a is the lattice constant), V is the unit-cell volume, and C, v_g, and τ denote specific heat, group velocity, and scattering time constant (lifetime), respectively. The integration is over all phonon wavenumbers from $\kappa = 0$ to $\kappa_{max} = \pi/(aA_x)$ [or $\pi/(aA_y)$] for branch m and the summation is over all the phonon branches; $\kappa = 2\pi/\lambda$, where λ is the wavelength. The nonvolumetric lattice thermal conductivity is denoted by K. The division by V stems from the fact that k is an intrinsic property.

The phonon specific heat C for each mode is computed according to the Bose–Einstein distribution



Mahmoud I. Hussein is the Alvah and Harriet Hovlid Professor at the Smead Department of Aerospace Engineering Sciences, University of Colorado Boulder. He also holds a courtesy appointment at the Department of Physics and an affiliated faculty appointment at the Department of Applied Mathematics. He received a B.S. degree from the American University in Cairo (1994) and M.S. degrees from Imperial College London (1995) and the University of Michigan, Ann Arbor (1999, 2002). In 2004, he received a Ph.D. degree from the University of Michigan, after which he spent two years at the University of Cambridge as a postdoctoral research associate. He is the founding Vice President of the International Phononics Society and a fellow of ASME. His research focuses on phononics at both the continuum and atomistic scales and theoretical studies of nonlinear wave motion.



Chia-Nien Tsai is a Ph.D. candidate and graduate research assistant at the Phononics Laboratory at the Smead Department of Aerospace Engineering Sciences, University of Colorado Boulder. He received his B.S. (2008) and M.S. (2010) degrees from the National Cheng Kung University, Taiwan. His Ph.D. dissertation focuses on computational simulation and analysis of nanophononic metamaterials.



Hossein Honarvar is a postdoctoral research associate at JILA and the Department of Physics, University of Colorado Boulder. Previously he was a Ph.D. student and graduate research assistant at the Phononics Laboratory at the Smead Department of Aerospace Engineering Sciences. He received his B.S. degree from the University of Tehran (2011) and M.S. degree from the University of New Mexico (2013). In 2016, he received the Teets Family Endowed Doctoral Fellowship at CU Boulder. His research interests include lattice dynamics and molecular dynamics of nanostructured materials and the study of thermal transport stemming from heat sources.

© 2019 WILEY-VCH Verlag GmbH & Co. KGaA, Weinheim

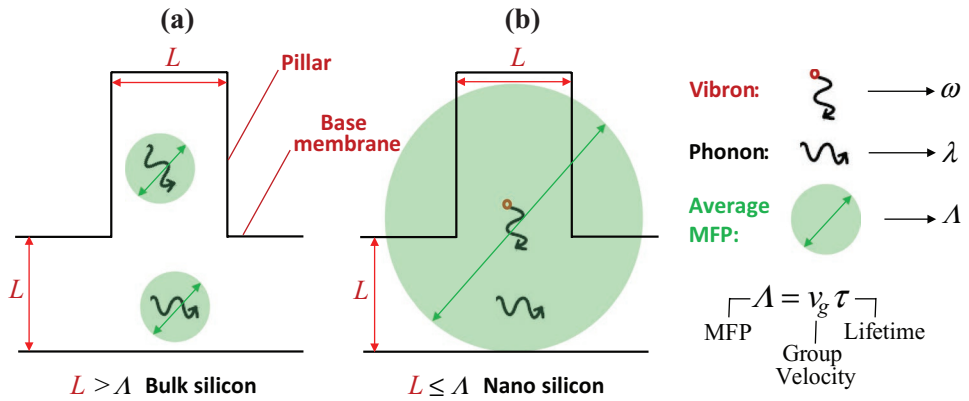


Figure 1. Schematic of a unit cell of a nanopillared silicon membrane. In this engineered structure, if the average MFP is smaller than the characteristic dimensions of the nanostructure, the medium behaves like a bulk material as shown in (a). On the other hand, if the average MFP (of the bulk material as a reference) is at least on the order of the feature sizes, then the system behaves as a nanostructured material as shown in (b). Temperature, among other factors, affect the average MFP. Also shown in (b) is a depiction of phonons in motion as traveling waves propagating along the base membrane and vibrons in motion as standing waves oscillating within the branching nanopillars. In contrast, in (a) only phonons are in motion; no vibrons exist.

$$C(\kappa,m) = k_B \frac{\chi^2 e^{\chi}}{(e^{\chi}-1)^2} \tag{2}$$

where k_B is the Boltzmann constant and $\chi = \chi(\kappa, m) = \hbar\omega/k_B T$, where T is the temperature, ω is the frequency, and $\hbar$ is the reduced Planck constant.

From Equation (1), it is seen that a prediction of k is constructed by summing over all phonon modes in the spectrum and integrating along the direction of interest over the Brillouin zone. The thermal conductivity is therefore dependent on the phonon band structure, which in turn is affected by the unit-cell structure and lattice symmetry. The integrand consists of a product of the specific heat, the group velocity squared, and the lifetime—all quantities defined for each mode of phonon motion as determined by the dispersion diagram. As discussed above, if the average MFP is smaller than the characteristic dimension—in this case the membrane thickness aA_z—then the relevant dispersion is primarily that of the primitive cell (consisting of two atoms) where the surfaces are nonexistent. When the thickness is on the order of the average MFP, then the in-plane dispersion of the membrane unit cell shown in Figure 2a is relevant and the effects of the surfaces are accounted for. The presence of the free surfaces also affect the phonon lifetimes due to boundary scattering, especially when the boundaries are rough.[14]

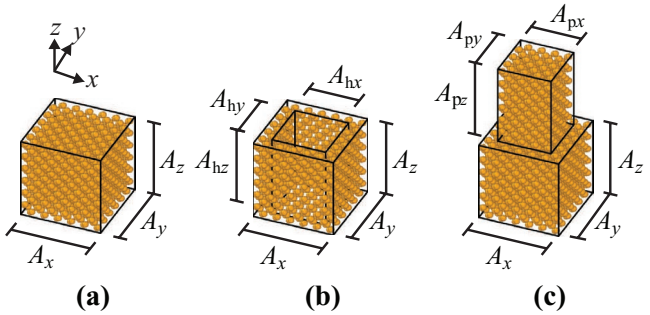


Figure 2. Atomic-scale models of a) uniform membrane, b) membrane-based nanophononic crystal, and c) membrane-based nanophononic metamaterial. Multiplying each dimension by a gives the length in nm.

2.2. Nanophononic Crystal

A phononic crystal is an artificial material with periodic features designed to enable controlled constructive and destructive interferences for elastic waves propagating through it.[15] This interferences mechanism, also known as Bragg scattering, takes form in a specific manner depending on the structure and symmetric arrangement of the unit cell. The dispersion diagram for the unit cell provides a rather comprehensive description of these effects. Applications of phononic crystals include vibration isolation,[16–19] wave focusing,[20,21] flow control,[22] topological insulators,[23,24] and nonreciprocal materials,[25–27] among others.[28–30] Downsizing a phononic crystal to the nanoscale brings rise to the notion of a nanophononic crystal. NPCs were first studied in the context of 1D layered materials, also known as superlattices,[31–35] but quickly were generalized to materials with 2D[5,6,36–40] and 3D periodicities.[41–43]

2.2.1. Membrane-Based NPC

One common configuration of an NPC consists of a host semiconducting material, silicon for example, forming a membrane with a periodic array of holes or inclusions patterned into it. The in-plane thermal conductivity of this system is also obtained by Equation (1) keeping in consideration that the phonon dispersion now is that of an NPC unit cell such as the one depicted in Figure 2b, and V is the volume of the NPC unit cell. While the interest in macroscopic phononic crystals is dominated by the presence of bandgaps, at the nanoscale (when a 3D crystal structure is modeled atomistically), a complete bandgap is unlikely to form.[42] This, however, is not a deterrent because the focus is primarily in the flattening of the dispersion curves. The flatter the dispersion curves, the lower the group velocities,

© 2019 WILEY-VCH Verlag GmbH & Co. KGaA, Weinheim

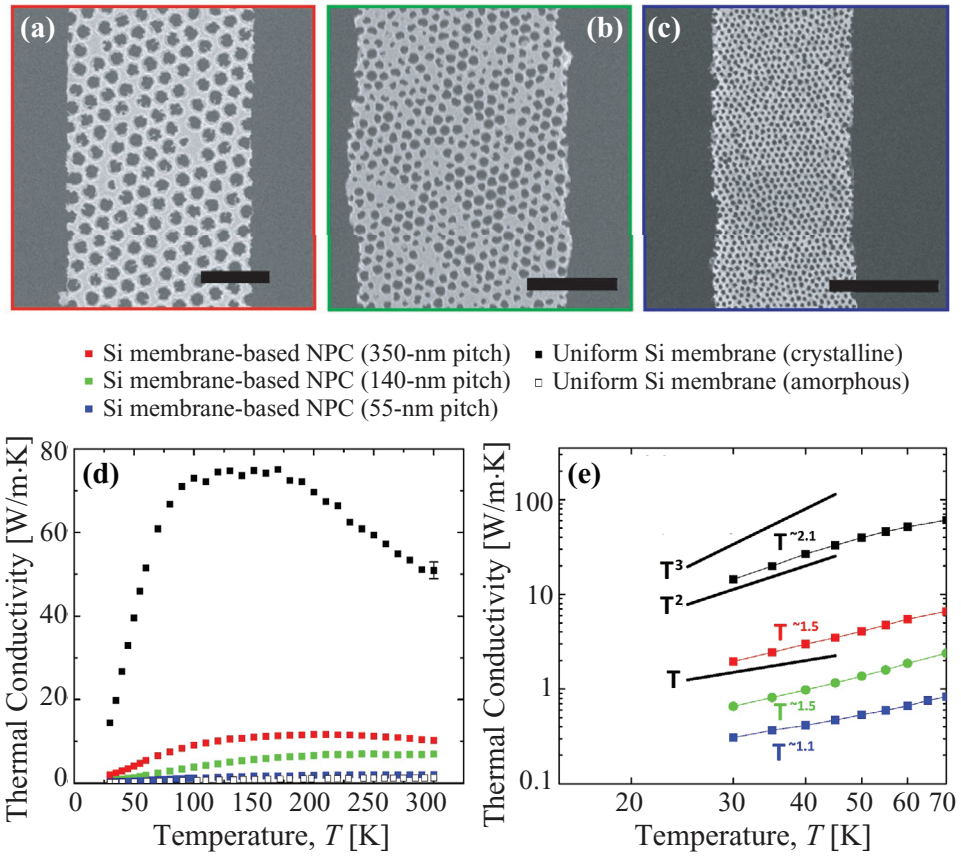


Figure 3. Thermal conductivity of silicon membrane-based NPCs with constant porosity and different pitch. SEM images of a) 350 nm pitch, b) 140 nm pitch, and c) 55 nm pitch NPC for thermal measurement (all scale bars are 1 μm wide). d) Temperature dependent thermal conductivity of uniform membrane (black squares), 350 nm (red squares), 140 nm (green squares), 55 nm pitch (blue squares) NPC membrane, and amorphous silica (empty squares from ref. [50]). Error bars for all three NPCs are smaller than the data points. e) Low-temperature data on a logarithmic scale with T^3, T^2, and T^1 curves for comparison. Adapted with permission.[5] Copyright 2010, American Chemical Society.

which, as seen in Equation (1), implies reduced thermal conductivity k.[44]

The NPC membrane of Figure 2b will exhibit a lower in-plane thermal conductivity compared to the corresponding uniform membrane of Figure 2a due to dispersion curves flattening. A practical challenge, however, is that the surfaces of the holes or inclusions need to be considerably smooth to preserve the phase information required for the Bragg effects to take place, especially when the characteristic dimensions of these holes or inclusions are of relatively large sizes compared to the phonon wavelengths.[40,45,46] More fundamentally, the degree and intensity of group-velocity reductions are limited to what the available Bragg interference patterns can provide, which is somewhat modest providing usually an order-of-magnitude reduction at most for unit cells with practical dimensions.[40] The boundaries or interfaces of the holes or inclusions may be roughened to increase the intensity of boundary scattering, possibly in combination with some level of Bragg scattering. In fact, the size and concentration of the holes or inclusions may be increased to the point where the phonon motion gets inhibited excessively by the scattering component leading to significant reductions in the thermal conductivity. However, this would be at the expense of having extremely small/thin segments in the host material (see ref. [43] for example) which would not be favorable if the interest is to reduce the thermal conductivity without negatively impacting the electrical conductivity, as needed in thermoelectrics.[47–49]

Figure 3 presents an example of a membrane-based NPC, investigated by Tang et al.[5] The NPC systems studied consisted of 100 nm thick silicon membranes with an array of nanoholes following a hexagonal pattern and a porosity of roughly $\phi = 35\%$. Three configurations were examined, having a pitch value of 350, 140, and 55 nm, respectively (see Figure 3 a–c). As shown in Figure 3d, the NPC systems exhibit a significant drop in the in-plane thermal conductivity—with the 55 nm pitch case dropping to values as low as 1.14–2.03 W m^{-1} K^{-1} compared to a peak value of nearly 75 W m^{-1} K^{-1} for a corresponding uniform membrane. Such small values of the thermal conductivity are much less than what is predicted for bulk silicon with the same porosity[5,51–53] and are comparable to that of amorphous silica.[50] A noticeable feature in the reported trends is that the peak of the thermal conductivity-versus-temperature curve (i.e., the Umklapp peak) is shifted to higher temperature as the pitch size decreases ($T_{U0peak} \approx 130$ K for uniform membrane,

© 2019 WILEY-VCH Verlag GmbH & Co. KGaA, Weinheim

$T_{U0peak} \approx 200$ K for 350 nm pitch NPC, and $T_{U0peak} > 300$ K for both 140 and 55 nm pitch NPC).[5] This indicates that phonon–phonon scattering across the unit cell decreases as the unit-cell size (given by the pitch) decreases. This is consistent with the discussion we provide above around Figure 1 as it shows that the NPC wave effects (Bragg scattering) indeed become more dominate with decrease in minimum feature size.

2.3. Nanophononic Metamaterial

The concept of a locally resonant metamaterial for the reduction of the thermal conductivity has been introduced by our group at the University of Colorado Boulder, first in 2014[2,3] and followed by a series of investigations adding further insight into the underlying physics and performance characteristics.[54–57] The basic principle in this new class of metamaterials—termed nanophononic metamaterial—is to create a medium consisting of a crystalline material, serving as a host, and an array of intrinsic substructures, serving as nanoresonators. Both the base material and the nanoresonators are made typically out of a semiconductor such as silicon. The local resonances of the substructures couple with the heat carrying phonons traveling nominally in the host material. This coupling brings rise to resonance hybridization between pairs of the wavenumber-independent vibration modes of the local substructure (vibrons) and wavenumber-dependent wave modes of the host medium (phonons). In this environment, the overall lattice thermal conductivity gets reduced by primarily three atomic-scale mechanisms. First, the phonon group velocities decrease at the coupling locations in the phonon band structure. Stronger couplings generate sharper curve flattenings and larger reductions in the group velocities. Second, the atomic motion within the nanoresonators gets localized at the resonance frequencies, which leads to further reduction in the thermal conductivity. Third, the phonon lifetimes decrease due to changes in the scattering environment, including both phonon–phonon scattering and boundary scattering. Shorter life times implies shorter mean free paths. If kept in moderation as to not disrupt the key wave mechanisms described above, this too contributes to the thermal conductivity reduction.[54,56]

The profound advantage of NPMs stems from the fact that the local resonances may be tuned by design to be numerous and to span the entire phonon spectrum of the host material. In the limit, the number of local resonances is three times the number of atoms in a unit nanoresonator. Moreover, the density-of-states (DOS) distribution of the vibrons may be tailored to highly conform to the DOS of the phonons traveling in the host material; see Section 3.2 for a demonstration and ref. [56] for an elaborate study of DOS conformity. Higher vibron–phonon DOS conformity intensifies the role of the local resonances. With these design attributes, it is possible to maximize the three effects mentioned above and achieve significant thermal conductivity reduction.

It is worth noting the fundamental difference with conventional metamaterials where the aim is to generate subwavelength bandgaps or create negative long-wave effective properties as is the case for locally resonant electromagnetic,[58,59] acoustic,[60] and elastic[61–64] metamaterials. In contrast, the aim in NPM design is to optimally enable the thermal conductivity reduction mechanisms: group velocities reduction, energy localization, and lifetimes reduction. Another key aim is to do so without affecting the electrical properties as this provides a unique opportunity to effectively increase the figure-of-merit ZT in thermoelectric energy conversion.[56,57]

2.3.1. Membrane-Based NPM

An NPM lends itself to a variety of configurations.[3] The architecture proposed in refs. [2,3,54–57] consists of a freestanding silicon membrane (or thin film) with an array of silicon nanopillars or nanowalls distributed on the surface(s); see unit-cell illustration in Figures 1 and 2c[65–67]. Here, the nanopillars/nanowalls act as the resonating substructures. This nanostructure allows us to leave the main body of the base membrane free of any voids or inclusions, unlike in an NPC as illustrated in Figure 2b. Since the membrane base serves as the transport zone, this layout is very favorable for electron generation and transport. The electronic band structure is only mildly affected and electron scattering occurs only near the membrane surfaces and not in the interior. Compared to all common phonon scattering-based approaches (where the scatterers are in the main body of the transport medium[68]), a nanopillared/nanowalled membrane therefore provides the unique advantage of practically decoupling the lattice thermal conductivity from the Seebeck coefficient and the electrical conductivity—which is essential to creating a significant increase in ZT. In addition, this NPM configuration naturally features dimensionality reduction (compared to the bulk form). Therefore, the powerful benefits of resonance-induced thermal conductivity reduction are gained over and above those of phonon confinement[65,66,69] and membrane surface roughness[14] (as well as the benefits to the electrical properties[70]).

Equation (1) applies to a membrane-based NPM as it does for a uniform membrane or a membrane-based NPC, using the NPM dispersion relation and keeping in consideration that for a nanopillared or nanowalled NPM, the volume V includes both the base membrane and nanopillar/nanowall portions. Recalling the three mechanisms that contribute to thermal conductivity reduction in an NPM, we see that reductions in the group velocities and lifetimes directly reduces the value of the integrand in Equation (1). As for the remaining factor of localization of modes, this impacts the thermal conductivity in a more subtle manner. While the nanopillar adds local modes (vibrons) to the total unit-cell system, most of these modes are strongly localized (i.e., exhibiting zero or near-zero group velocity in the band structure). Therefore, even though these modes add to the number of terms summed in Equation (1), the actual additional quantities that are summed are not significant. Since the full integration is finally divided by the total unit-cell volume, the net effect on the thermal conductivity is that it decreases. **Figure 4** provides a visual depiction of a localized mode in a membrane-based NPM. It is clear that the atomic motion in the base membrane of the NPM is almost stagnant (right portion of the figure), and thus carries very little heat. This is in stark contrast to the corresponding mode for a uniform (unpillared) membrane, as also shown (left portion of the

© 2019 WILEY-VCH Verlag GmbH & Co. KGaA, Weinheim

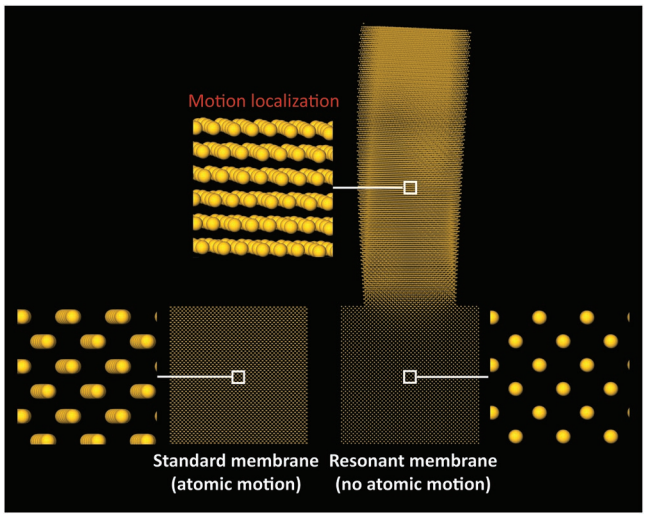


Figure 4. Demonstration of mode localization in a membrane-based NPM. Adapted with permission.[56] Copyright 2018, American Physical Society.

figure). Honarvar and Hussein[56] investigated by equilibrium molecular dynamics (MD) simulations an all-silicon 9.78 nm thick membrane with 586.5 nm tall nanopillars covering 79% of the surface area on both sides, and reported a room-temperature thermal conductivity reduction of a factor 130 compared to a corresponding uniform membrane. This is equivalent to a reduction of a factor of 481 compared to bulk crystalline silicon and nearly a factor of 2 compared to bulk amorphous silicon. With some elementary calculations, this amounts to a projection of a ZT value higher than 3,[56] or possibly in excess of 4 with optimal doping.[57]

2.3.2. Growth of NPM Research

Since the first publication on NPMs in 2014,[2] several investigations followed exploring a variety of configurations. Most studies have used computer simulations to assess the impact of NPM material properties and geometric features on the thermal conductivity. Using atomic-level modeling, Wei et al. studied the effects of varying the nanopillars spacing and dimensions in silicon nanopillared membranes and analyzed mode localization.[71] Silicon NPMs in the form of rods/wires with branching substructures were considered by Xiong et al.[72] where they explored the effects of temperature and the impact of alloying; see **Figure 5**. It is observed that the NPM exhibits a lower thermal conductivity than the uniform case by a factor of nearly 3 at room temperature and just less than 2 at 800 K. As the temperature increases, the intensity of anharmonic phonon–phonon scattering increases (leading to reductions in the MFPs) and this in turn reduces the effect of the local resonances. However, the less steep—but clear—downward trend of k versus T for the silicon NPM is indicative that there is still room for additional scattering with increasing temperature. This provides indirect evidence that while the nanoresonators increase the scattering environment, they do so in moderation. Honarvar and Hussein also examined the

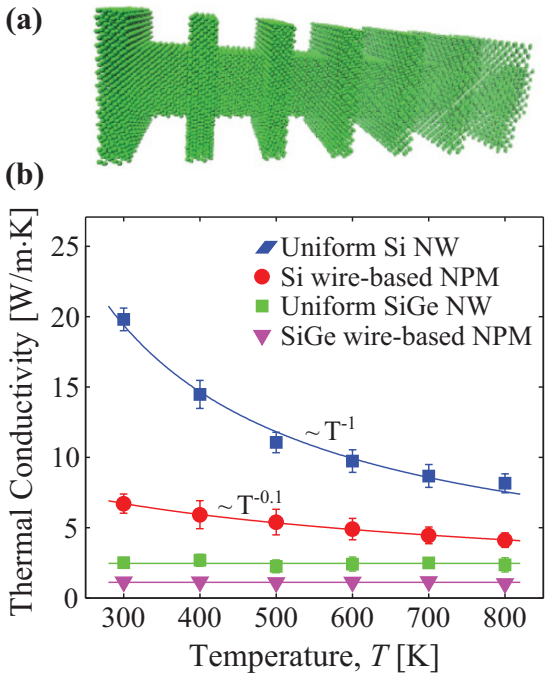


Figure 5. Lattice thermal conductivity along the axial direction in a wire-based NPM. The nanoresonator takes the form of a nanowall with a square axial cross-section that fully surrounds the base wire. The dimensions are as follows: wire thickness is 4.34 nm; unit-cell length (pitch) is 2.17 nm; nanowall axial width is 1.09 nm; nanowall branching height is 1.63 nm. a) Atomic model, and b) thermal conductivity versus temperature for silicon and $Si_{0.5}Ge_{0.5}$ wire-based NPMs and corresponding uniform wires. Adapted with permission.[72] Copyright 2016, American Physical Society.

effect of temperature.[56] For the 9.78 nm thick membrane with 586.5 nm tall double-sided nanopillars, a prediction of a factor of 19 reduction in the thermal conductivity was reported at T = 700 K; in contrast to the factor of 130 predicted at T = 300 K. Regarding alloying, Xiong et al.[72] demonstrated that one of their silicon wire-based NPM experiences a factor of slightly less than 3 reduction in k with the resonances effect and an additional factor of nearly 7 by alloying with 50% germanium atoms—providing a total reduction of a factor of ≈20 at T = 300 K. Further investigation of rod/wire-based NPMs has appeared recently.[73]

Ma et al. investigated local resonant effects in 3D silicon nanowire cages,[74] and Zhu et al.[75] considered bulk silicon with internal amorphous regions acting as an environment of nanoresonators (see ref. [76] for a survey of potential configurations using atomically disordered inclusions). The notion of a surface oxidized membrane acting as an NPM—with the disordered oxygen atoms covering the membrane surface acting as the nanoresonators—was proposed by Xiong et al.[77] NPMs in the form of branched nanoribbon materials composed of molybdenum disulfide (MoS_2) were studied by Liu et al.[78] Giri and Hopkins[79] and Yang and co-workers[80] extended the NPM concept to carbon nanotubes and graphene sheets, respectively. Another intriguing NPM architecture is based on a graphene sheet with branching fullerene nanoresonators.[81] Other than thermal conductivity reduction, the impact of nanopillars on the

© 2019 WILEY-VCH Verlag GmbH & Co. KGaA, Weinheim

heat capacity was investigated by Iskander et al. using both theory and experiments.[82] NPMs have also been employed for thermal rectification, in indium arsenic (InAs) nanowires,[83,84] nanopillared graphene structures,[85] and graphene nanoribbons.[86] A range of possible NPM geometric configurations, including 1D, 2D, and 3D systems is given in ref. [3], noting that one of the unique features of NPMs is that they may be realized using a wide range of constituent materials for both the host medium and the nanoresonator medium.

Nanophononic metamaterials have also been studied using finite-element (FE) analysis as commonly done for macroscale acoustic or elastic metamaterials.[87–91] However, while linear continuous modeling may provide some insight on the dynamics of local resonances, nonlinear atomic-scale models are necessary for accurate qualitative and quantitative capturing of the effects of the three key NPM mechanisms responsible for the thermal conductivity reduction. This can be seen in the inherent dependence of the thermal conductivity on 1) the number, range, and detailed characteristics of the dispersion branches in the phonon band structure, as evidenced in Equation (1) and the intricate band structure of NPMs (as shown in Section 3), and 2) the anharmonic interatomic interactions. A study of the convergence of the FE-based thermal conductivity reduction predictions to those obtained by atomic modeling is given in the Supporting Information accompanying ref. [2]. The importance of atomic resolution and nonlinear effects is further noted by evidence of significant size and geometry dependence of the underlying physics of nanoscale thermal conduction in NPMs.[56]

Experimental investigation of NPMs is at its early stage. Spann et al. presented preliminary results for 200 nm thick silicon membranes with gallium-nitride nanopillars grown by molecular beam epitaxy—ranging in height from 1 to 4 μm and covering roughly 55% of the surface area—and reported a nearly 25% reduction in the thermal conductivity.[92] The thermal conductivity was measured by Raman thermometry.[93–95] A recent paper by Maire et al.[96] examined all-silicon suspended wires with nanowalls fabricated by means of electron beam lithography and inductively coupled plasma reactive-ion etching and characterized by a time domain thermoreflectance technique.[97–99] They considered a range of dimensions of wire thickness, nanowall dimensions, and gap size between the nanowalls. **Figure 6** shows the relationship between the measured thermal conductivity and the nanowall width for varying wire thickness (fixing the other cross-sectional dimension of the wire to 145 nm). The trends clearly demonstrate an improvement in the reduction in the thermal conductivity with larger nanoresonators and smaller base-wire thickness—which is consistent with the theoretical NPM performance trends discussed in Section 2.3 and computationally demonstrated in ref. [56].

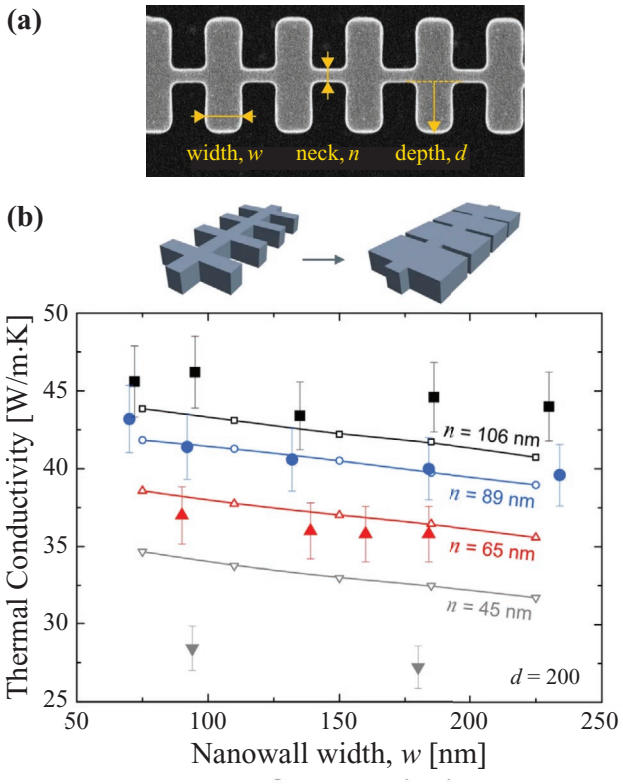


Figure 6. Experimental investigation of the axial thermal conductivity in an all-silicon wire-based NPM with branching nanowalls. a) SEM close-up image of the NPM, and b) thermal conductivity versus nanowall width for samples with different wire thickness (neck size, n) and the same nanowall height (depth, d = 200 nm) and unit-cell length (pitch, p = 300 nm). Measurements are represented by discrete data points, and results obtained by simulations are plotted by solid lines with dots. Adapted with permission.[96] Copyright 2018, Springer Nature; the notation used is applicable only to this figure.

2.4. NPM versus NPC

In this review article, we pay particular attention to the thermal transport properties of NPMs compared to NPCs and we do so with a view on their performance potential as thermoelectric materials. Unlike NPCs, NPMs do not depend on periodicity and phased wave interferences, and are therefore more robust to disorder in the arrangement of their key component—the nanoresonators—and to surface roughness. In addition, and very importantly, the intensity of group-velocity reductions, mode localizations, and controlled lifetime reductions—the key mechanisms in NPMs—may be continuously enhanced by simply increasing the size and packing efficiency of the nanoresonators.[56,71] This unique quality takes effect without diminishing the advantage that in a nanopillared or nanowalled membrane configuration the branching nanoresonators are located outside the path of the electrons—and are therefore not expected to cause much changes to the electrical properties, as discussed above. As we show in this paper, NPCs on the other hand do not enjoy a similar level of design freedom with its key mechanism of Bragg scattering.

The fundamental differences between NPMs and NPCs are investigated in the next two sections. In Section 3, we use equilibrium MD simulations followed by Fourier transform in space and time to recover the phonon band structure for an NPM in the form of a nanopillared membrane and an NPC in the form of a "holey" membrane with the same membrane thickness. The same analysis is done for a corresponding

© 2019 WILEY-VCH Verlag GmbH & Co. KGaA, Weinheim

uniform membrane as a reference. In Section 4, a parametric study is conducted comparing the thermal conductivity of these NPM and NPC configurations. The effect of both nanopillar/nanohole size is investigated, and for the NPMs, three different nanopillar heights are considered. We also examine in Section 4 the effect of the in-plane unit-cell size on the thermal conductivity reduction in the four systems and provide a comparative analysis. A summary and outlook are presented in Section 5.

3. Phonon Band Structure of NPM versus NPC

3.1. Unit-Cell Configurations

In this section, we consider an NPM in the form of a periodic nanopillared membrane and compare its phonon band structure with that of an NPC in the form of a periodic nanoholed membrane. The phonon band structure of a uniform membrane is also obtained to serve as the reference configuration for both nanostructured materials. Following the notation depicted in Figure 2, we consider a unit-cell model of a suspended membrane with dimensions $A_x \times A_y \times A_z$ conventional cells (CC); see Figure 2a. A silicon CC consists of eight atoms packaged as a cube with a side length of $a = 0.5431$ nm. For the NPC unit cell, we drill a hole through the entire thickness, and for the NPM unit cell, we erect a nanopillar on top of the base membrane portion. Both the nanohole and nanopillar are centrally positioned in the respective unit cell. The dimensions of the NPC nanohole and the NPM nanopillar are $A_{hx} \times A_{hy} \times A_{hz}$ CC and $A_{px} \times A_{py} \times A_{pz}$ CC; see Figure 2b,c, respectively.

To allow for direct comparisons, we set the base dimensions of all unit cells to be identical, $b = aA_x = aA_y$ nm. Similarly, we set the thickness of all unit cells to be equal, $d = aA_z$ nm. Furthermore, the width of the nanoholes and nanopillars are also chosen to be equal, in both the x- and y-directions, that is, $c = aA_{hx} = aA_{hy} = aA_{px} = aA_{py}$ nm. As mentioned earlier, the nanoholes penetrate through the entire NPC unit cell. Three nanopillar heights are considered for the NPMs: $h = h_1 = aA_{pz}$ nm for NPM_1, $h = h_3 = 3aA_{pz}$ nm for NPM_3, and $h = h_{60} = 60aA_{pz}$ nm for NPM_{60}. These geometries are depicted in **Figure 7** for visualization.

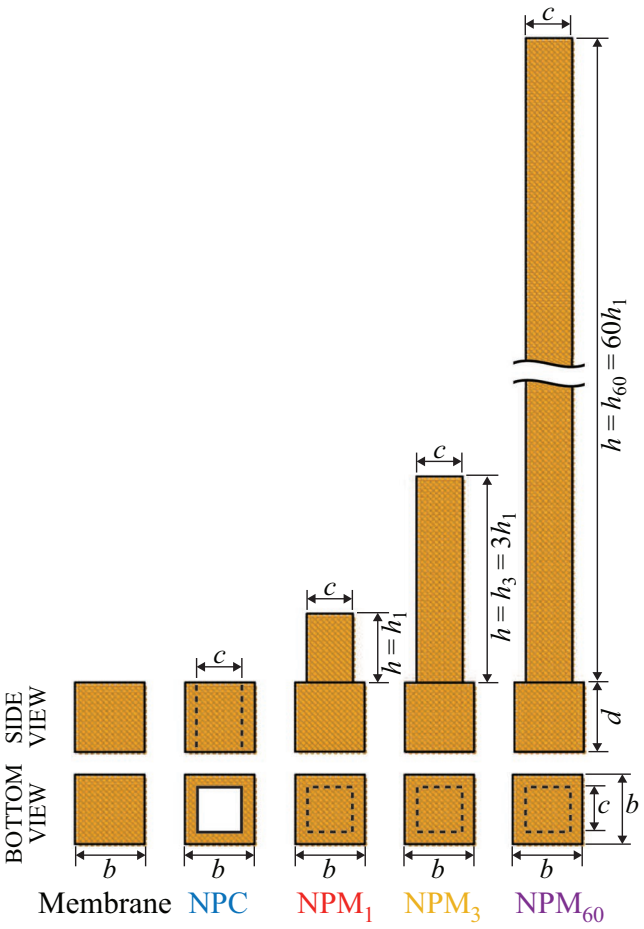


Figure 7. Schematics representing the five membrane-based material systems considered in this investigation. NPM_1, NPM_3, and NPM_{60} are identical except for the nanopillar heights. The width of the nanoholes in NPC is identical to the width of the nanopillars. All membranes have identical base dimensions and thickness.

3.2. Lattice Dynamics, Molecular Dynamics, and Spectral Energy Density

All analysis in this paper is done using atomic-scale models. In all models, room temperature at $T = 300$ K is assumed and the Stillinger–Weber empirical potential is used to represent the interatomic interactions.[100]

3.2.1. NPM Phonon Band Structure

The phonon band structure is first obtained by quasiharmonic lattice dynamics (LD) calculations.[101] While these eigen-analysis calculations do not take into account the anharmonicities in the interatomic potential, they provide a robust characterization of the linear wave propagation modes admitted in a given periodic system. Accounting for nonlinear effects, however, is essential because phonon–phonon scattering—which is a nonlinear phenomenon—stands as a key competing process to the very wave mechanisms that both NPCs and NPMs depend on for exhibiting their unique properties. Therefore, we complement our LD results with phonon band structures extracted directly from MD simulations where the anharmonicities are fully retained. This latter calculation effectively involves a Fourier transformation of the MD velocity field to obtain a frequency-versus-wavenumber map of the spectral energy density (SED).[102–105] MD simulations are also used to obtain the key quantity of interest, which is the in-plane thermal conductivity (see Section 4).

The MD simulations are performed under equilibrium conditions using the LAMMPS software.[106] The MD systems are initially equilibrated for 1 ns, with a time step $\Delta t = 0.5$ fs, at $T = 300$ K under the *NPT* ensemble (zero pressure cell size based on constant number of atoms, pressure, and temperature). This phase of the simulations allows the atoms to reach equilibrium and

© 2019 WILEY-VCH Verlag GmbH & Co. KGaA, Weinheim

causes a reconstruction of the surfaces due to boundary atoms relaxation.[107] The simulations are subsequently allowed to run under the *NVE* ensemble (constant number of atoms, volume, and energy) for either calculation of the thermal conductivity using the Green–Kubo method (as described in Section 4) or the SED distribution as a function of frequency and wavenumber. For the SED calculations, the *NVE* simulations are run for 2^{22} time steps covering 2 ns, and information is extracted every 2^5 steps. Both sets of *NVE* calculations are based on $\Delta t = 0.5$ fs as earlier.

The SED distribution is calculated by evaluating the expression, Φ', which is a function of wave vector $\boldsymbol{\kappa}$ and frequency ω. For our all-silicon system, this expression is given by ref. [102].

$$\Phi'(\kappa,\omega) = \mu_0 \sum_{\alpha}^{3} \sum_{b}^{n} \left| \sum_{l}^{N} \int_{0}^{\tau_0} \dot{u}_\alpha \begin{pmatrix} l \\ b \end{pmatrix}; t \right) e^{i\left[\boldsymbol{\kappa}\cdot\mathbf{r}_0\begin{pmatrix} l \\ 0 \end{pmatrix} - \omega t\right]} dt \Bigg|^2 \quad (3)$$

where $\mu_0 = m/(4\pi\tau_0 N)$, m is the mass of a silicon atom, τ_0 is the total simulation time, $\mathbf{r_0}$ is the equilibrium position vector of the lth unit cell, and $\dot{u}_\alpha$ is the α-component of the velocity of the bth atom in the lth unit cell at time t. There are a total of $N = N_x \times N_y \times N_z$ unit cells in the simulated computational domain with n atoms per unit cell. It is noted that in Equation (3), the phonon frequencies can only be obtained at the set of allowed wave vectors as dictated by the crystal structure. For our model, the ΓX-path wave vectors are $\kappa_x = 2\pi j/(N_x A_x)$, $j = 0$ to $N_x/2$, where $N_x = 50$ and $N_y = N_z = 1$. Standard periodic boundary conditions are applied at the far-end boundaries in the in-plane directions, and the upper and lower surfaces are left free. The ΓX wave-vector resolution is $\Delta\kappa_x = 0.04$.

In **Figure 8**, we show the phonon band structure of a uniform membrane, a membrane-based NPC, and a membrane-based NPM based on LD (solid red curves) and SED (color contour). The systems are represented by the first three unit cells depicted in Figure 7, including NPM_1. For the band-structure calculations, the following dimensions are selected: $b = d = h = 3.2586$ nm [$b/a = d/a = h/a = 6$ CC], and $c = 2.1724$ nm [$c/a = 4$ CC]. First, we note from Figure 8a that the SED results are in good agreement with the LD curves; this 1) provides verification for the MD simulations and subsequent SED calculations, and 2) indicates that the effects of anharmonicities on the phonon band structure are relatively small in room-temperature silicon. Second, the NPC curve flattenings due to Bragg scattering are observed in the SED results in Figure 8b. Third, the NPM local resonances, or vibrons, appear as horizontal lines in the SED results in Figure 8c—this feature represents the key signature of an NPM. It is also noted that the vibron lines couple with the underlying phonon dispersion curves associated with the base membrane, thus causing the resonance hybridizations effect that reduces the group velocities of the heat carrying modes. Both the Bragg-scattering curve flattenings and the local resonances are well aligned with the corresponding LD curves. This provides unequivocal evidence that wave behavior is indeed present in both these nanostructures at room temperature, despite the presence of anharmonic phonon–phonon interactions and possible scattering by the relaxed boundaries.

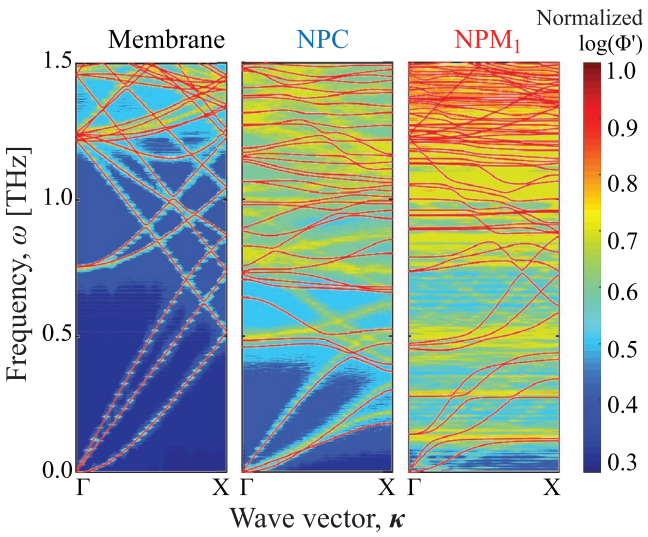


Figure 8. Phonon dispersion of a) a uniform membrane, b) a membrane-based NPC, and c) a membrane-based NPM, all with the same membrane thickness. The solid lines represent the dispersion curves obtained directly from quasiharmonic LD calculations; the color contours represent the SED spectra, which are each normalized by the corresponding maximum value. Since there is a high concentration of dispersion curves at higher frequencies, only a small low-frequency portion of the spectrum is displayed. A similar analysis is covered in detail in ref. [54].

3.2.2. Phonon–Vibron DOS Conformity

As mentioned in Section 2.3, a key factor for the local resonances effects to materialize and impact NPM performance is the degree of conformity between the vibrons DOS distribution of the nanoresonantor (e.g., nanopillar or nanowall) and the

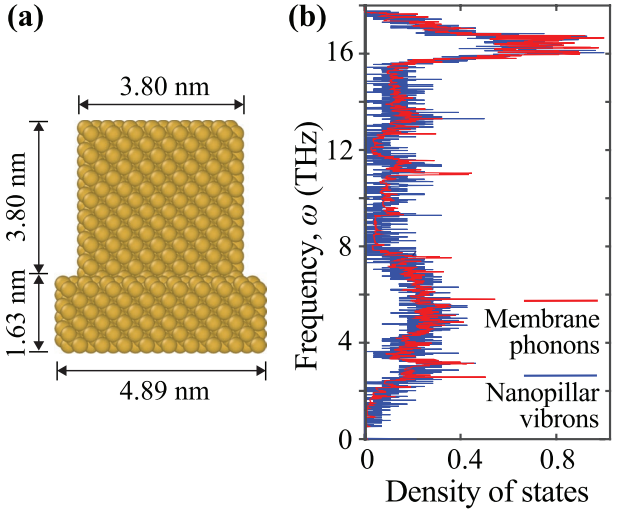


Figure 9. Demonstration of near-perfect phonon–vibron conformity of DOS distributions for a large nanopillar standing on a thin base membrane in an all-silicon NPM. a) Schematic of NPM atomic model, and b) frequency distribution of the DOS for base membrane phonons and the nanopillar vibrons, when each is viewed in separation. The vibron DOS are obtained by considering the nanopillar as an independent nanostructure with free boundary conditions. All quantities are normalized with respect to their maximum values. Adapted with permission.[56] Copyright 2018, American Physical Society.

© 2019 WILEY-VCH Verlag GmbH & Co. KGaA, Weinheim

phonons DOS distribution of the transport medium (e.g., base membrane). The DOS distributions may be evaluated for each component in separation or as part of the overall NPM. The higher the degree of conformity of these two DOS quantities, the more effective are the three effects induced by the local resonances. Having a high net intensity of vibrons (by having a large nanoresonator volume) is in itself highly favorable. However, the vibrons are most influential when they fall within the same regions of the phonons in the frequency spectrum. In **Figure 9**, we demonstrate an extremely high degree of phonon–vibron DOS conformity for a well-designed membrane-nanopillar NPM. As described and elucidated in ref. [56], the ratio of the volume of the nanopillar to that of the base membrane is directly proportional to the degree of phonon–vibron DOS conformity. It was also shown that for a given volume of the nanopillar, its width had a slightly higher impact on the conformity than its height. Having both the membrane and the nanopillar fabricated out of the same constitute material naturally also increases the phonon–vibron DOS conformity.

4. Geometric and Size Effects: NPM versus NPC

To enable an equitable and informative comparison between NPMs and NPCs, it is essential to keep the value of certain geometric parameters constant between the two configurations and vary other parameters in a consistent manner. In this section, we report on two comparative studies featuring membrane-based NPMs, membrane-based NPCs, and, as a reference case, a uniform membrane. The membrane thickness is a common geometric feature between these three nanostructures and is used to provide the link as other geometric features and feature dimensions are varied. In Section 4.1, we give the details of our modeling, simulations, and thermal conductivity prediction approach. In the subsections that follow, we provide results pertaining to the effects of varying nanohole/nanopillar width for a given unit-cell size (Section 4.2) and varying unit-cell lateral dimension for a given ratio of nanohole/nanopillar width to unit-cell size (Section 4.3). In both investigations, the effect of the nanopillar height is also examined by considering three ratios of nanopillar height to base-membrane thickness.

4.1. Thermal Conductivity Prediction by Equilibrium MD and the Green–Kubo Method

For the thermal conductivity predictions, a single unit cell is considered, i.e., $N_x = N_y = N_z = 1$, to form the computational domain, and standard periodic boundary conditions are applied in the in-plane directions while keeping the upper and lower surfaces free. Equilibrium MD simulations are run using the same interatomic potential as used in the previous section. As mentioned in Section 3, *NPT* simulations are first run for 1 ns, with a time step $\Delta t = 0.5$ fs, to reach equilibrium at room temperature. For k predictions, this is followed by *NVE* runs for 1.2×10^7 time steps covering 6 ns, during which heat fluxes are collected every 4 fs. The 6 ns time span is sufficiently long compared to the longest phonon lifetime to reliably predict k.

The in-plane lattice thermal conductivity is then calculated using the Green–Kubo method[108–112]

$$\boldsymbol{k} = \frac{1}{k_B V T^2} \int \langle \boldsymbol{J}(0) \otimes \boldsymbol{J}(t) \rangle \, \mathrm{d}t \tag{4}$$

where V is the total volume of the unit cell (base membrane minus the nanohole for NPCs and base membrane plus nanopillar for NPMs), $\boldsymbol{J}$ is the heat current vector computed over all atoms in the system, and $\otimes$ denotes the tensor product operation. The heat current vector is evaluated using the stress-based formula $\boldsymbol{J} = -\sum \boldsymbol{S}_i \boldsymbol{v}_i$, where $\boldsymbol{S}_i$ and $\boldsymbol{v}_i$ denote the virial stress tensor and the velocity vector for atom i, respectively.[106] The integrand $\langle \boldsymbol{J}(0) \otimes \boldsymbol{J}(t) \rangle$ represents the time average of the HCACF.

All reported thermal conductivities are obtained by running six independent simulations with different initial velocities and considering transport along both the x- and y-directions along the plane. From the 12 independent results, a systematic statistical analysis is conducted considering all possible combinations of eight (out of 12) realizations and a thorough ranking procedure based on temporal convergence of k over a fixed window in time.

4.2. Thermal Conductivity versus Nanohole/Nanopillar Lateral Size for Fixed Unit-Cell Base Dimensions

The two key dimensions in the NPM configurations shown in Figure 7 are the nanopillar width c and height h. These two parameters are influential especially when viewed relative to the base membrane dimensions of b and d. Thus, we define a volume fraction V_r to quantify the relative volume of the nanopillar with respect to the volume of the base membrane[56]

$$V_r = \frac{V_{\text{Pillar}}}{V_{\text{Base}}} = \frac{c \times c \times h}{b \times b \times d} \tag{5}$$

To examine the impact of the nanohole/nanopillar dimensions on the thermal conductivity reduction, we consider the three NPM configurations depicted in Figure 7, namely NPM_1, NPM_3, and NPM_{60}, and the NPC uniform membrane configuration also depicted in the figure. We investigate varying the nanohole/nanopillar width c while keeping b and d constant. The in-plane thermal conductivity is calculated for the cases listed in **Table 1**. For each case, we report the ratio of the thermal conductivity of the nanostructure NPX (X = C for NPC

Table 1. Width effect: Choice of dimensions for thermal conductivity predictions plotted in Figure 10.

Configuration	b/a [CC]	c/a [CC]	d/a [CC]	h/a [CC]
Membrane	18	N/A	18	N/A
NPC	18	2,4,...,16	18	N/A
NPM_1	18	2,4,...,16	18	18
NPM_3	18	2,4,...,16	18	54
NPM_{60}	18	2,4,...,16	18	1080

© 2019 WILEY-VCH Verlag GmbH & Co. KGaA, Weinheim

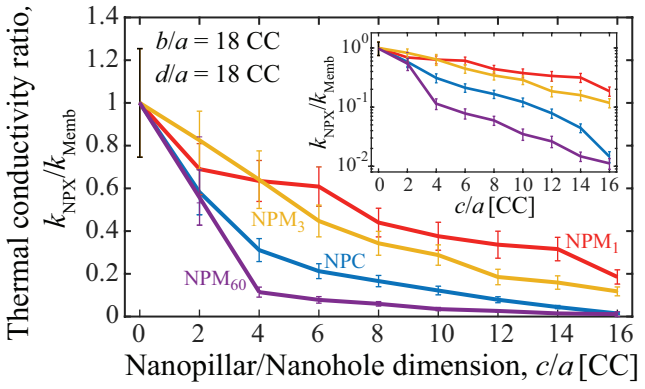


Figure 10. Effect of varying nanohole/nanopillar lateral size: Thermal conductivity reduction versus nanopillar width for three membrane-based NPMs with different nanopillar heights but a fixed membrane thickness and a fixed separation distance between the nanopillars. A comparison is provided for a corresponding membrane-based NPC where the hole width is varied in the same way. Schematics of all four unit cells are given in Figure 7. All results are normalized with respect to the thermal conductivity of a uniform membrane with the same thickness. All results are for $b = d = 9.78$ nm. Inset shows same results with the thermal conductivity reduction plotted in log scale.

and X = M for NPM) to the thermal conductivity of a uniform membrane with the same thickness. The results are plotted in **Figure 10** and tabulated in **Table A1** in the Appendix.

The first observation is that as each of c and h increases, the value of k_{NPM}/k_{Memb} decreases. This is consistent with the results of Honarvar and Hussein[56] and is explained by the increase in V_r. As mentioned earlier, the increase of V_r has two advantages: 1) the phonon band structure gets enriched with a higher vibrons-to-phonons ratio, and 2) the level of conformity between the phonons and vibrons DOS distributions gets significantly enhanced. Both these effects are highly favorable for reducing the thermal conductivity because they increase the intensity of the three NPM mechanisms discussed earlier, namely, the group-velocity reductions, the mode localizations, and the lifetime reductions near the hybridization zones.[56] Populating the spectrum with numerous, DOS-conforming vibrons is particularly important at the bottom half of the spectrum because this is where the heat carrying phonons contributing most to the thermal conductivity reside.[2]

The second key observation we make from Figure 10 is concerning the NPM versus NPC performance. The NPC unit cell shows a firm reduction in the thermal conductivity with increase in nanohole width. This is because a large nanohole causes more Bragg scattering and boundary scattering. Clearly the NPC system outperforms both NPM$_1$ and NPM$_3$ for all values of c/a. However, when the nanopillar is extended to a significant height, the outcome flips. We see that NPM$_{60}$ outperforms NPC, and does so at all values of c/a above 2 CC[113]. This is a significant result because the base membrane component in NPM$_{60}$ is all solid and has no obstacles of any type for the generation and transport of electrons, which is very favorable for thermoelectric energy conversion. It is remarkable to see that with an extremely narrow nanopillar of side dimension $c/a = 4$ CC, k_{NPX}/k_{Memb} for NPM$_{60}$ is less than a third of that for the corresponding NPC configuration with a nanohole of the same side dimension. For the very wide nanohole/nanopillar width of $c/a = 16$ CC, NPM$_{60}$ experiences nearly 60% of the thermal conductivity of NPC. The k_{NPC}/k_{Memb} value of NPC with $c/a = 14$ CC (a very large nanohole) roughly matches the k_{NPM}/k_{Memb} value of NPM with $c/a = 8$ CC (a nanopillar with nearly half the width of the nanohole).

The lowest reported thermal conductivity in Figure 10 is $k_{NPM}/k_{Memb} = 0.009 \pm 0.002$, which is for NPM$_{60}$ that has a volume fraction of $V_r = 47.4$. This reduction is nearly 50% stronger than the value reported in ref. [56] for the same system, but the two predictions overlap in their error-bar windows[14,113–116]. Further significant reduction in k_{NPM}/k_{Memb} is expected if 1) another nanopillar is added to the bottom side of the membrane, and 2) if the nanopillars are stretched along the direction perpendicular to the thermal transport and transformed into "nanowalls."[56] These enhancements would raise the V_r value of the NPM$_{60}$ configuration to $V_r = 94.8$ and $V_r = 53.3$, respectively. If both enhancements are implemented simultaneously, we get $V_r = 106.7$. Future investigations may examine the performance of such elevated V_r systems.

Other mechanisms could be employed for additional reduction in the thermal conductivity; for example, alloying the base membrane portion to introduce some mild scattering that is significant enough to reduce k_{NPM}/k_{Memb} but also not too strong to impede the resonance effects.[72]

4.3. Thermal Conductivity versus Unit-Cell Base Size for Fixed Nanohole/Nanopillar Filling Fraction

From a practical point of view, NPMs at present are realizable in sizes substantially larger than the cases considered in this paper. This is owing to feasibility considerations for nanofabrication[118] and efficient device integration.[119] With the continued development of high-capacity computing, NPM unit cells of larger sizes will be investigated in the future. In the meantime, it is beneficial to examine the relative trends in performance for various computationally tractable NPM configurations (and a corresponding NPC for comparison) as the overall size increases. The NPM size factor has been investigated by the authors in two prior publications.[55,56] Here, we build on these investigations and examine the effect of proportionally increasing the unit-cell size specifically along the planar directions.

Once again, we consider the NPM$_1$, NPM$_3$, NPM$_{60}$, and NPC nanostructures. Now we investigate varying the base membrane

Table 2. Size effect: Choice of dimensions for thermal conductivity predictions plotted in Figure 11.

Configuration	b/a [CC]	c/a [CC]	d/a [CC]	h/a [CC]
Membrane	18	N/A	18	N/A
NPC	6,9,...,18	4,6,...,12	18	N/A
NPM$_1$	6,9,...,18	4,6,...,12	18	18
NPM$_3$	6,9,...,18	4,6,...,12	18	54
NPM$_{60}$	6,9,...,18	4,6,...,12	18	1080

© 2019 WILEY-VCH Verlag GmbH & Co. KGaA, Weinheim

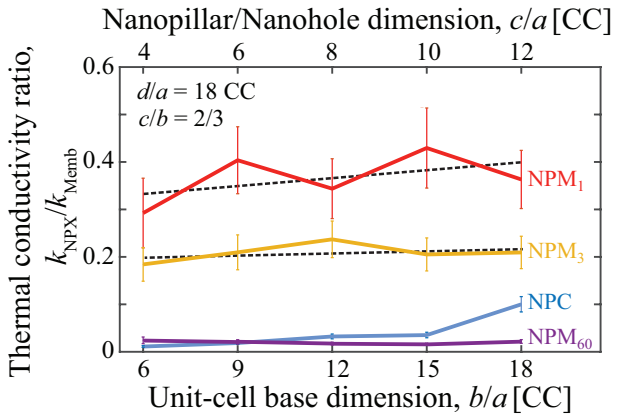


Figure 11. Effect of varying unit-cell base size: Thermal conductivity reduction versus separation distance between nanopillars for three membrane-based NPMs with different nanopillar heights but a fixed membrane thickness. A comparison is provided for a corresponding membrane-based NPC where the separation distance between the nanoholes is varied in the same way. Schematics of all four unit cells are given in Figure 7. All results are normalized with respect to the thermal conductivity of a uniform membrane with the same thickness. All results are for $d = 9.78$ nm and $c/b = 2/3$.

width b while keeping d constant and the ratio c/b fixed to 2/3. These variations in dimension keep the V_r value fixed for each configuration to 0.67 for NPM_1, 1.34 for NPM_3, and 26.67 for NPM_{60}. The in-plane thermal conductivity is calculated for the cases listed in **Table 2**. For each case, we also report k_{NPX}/k_{Memb}. The results are plotted in **Figure 11** and tabulated in **Table A2** in the Appendix. The case of $b/a = 18$ CC and $c/a = 12$ CC is a common data point with the Figure 10 results, but has been resimulated here to maintain consistency in the statistical treatment of the data within each figure.

It is observed that as the size of NPM_1 is proportionally increased in the lateral directions, the thermal conductivity ratio k_{NPM}/k_{Memb} drifts slightly upward. This trend is consistent with previously reported predictions,[55,56] and is attributed to deterioration in the degree of vibron–phonon DOS conformity as the unit-cell size increases while keeping V_r fixed. However, as also observed in these aforementioned earlier studies, this deterioration is less significant for NPM unit cells with larger volume fractions. Indeed this is noticed in Figure 11 when examining the slope of the rise of k_{NPM}/k_{Memb} for the various NPM configurations. NPM_3 experiences a milder rise compared to NPM_1, and NPM_{60} experiences no noticeable change as the lateral size of the unit cell is increased. As reported by Honarvar and Hussein,[56] the slope of the k_{NPM}/k_{Memb} trend with size may be rendered negative when the volume of the nanopillar is increased at a higher rate as the volume of the base-membrane portion is increased. This phenomenon has been described as the "compensatory effect."

The NPC thermal conductivity reduction is shown to also deteriorate with increase in lateral size. This is attributed to changes to the Brillouin zone size (which directly affects Bragg scattering). It is also affected by changes in the ratio $4c/b^2$, which is the ratio of the internal perimeter of the nanohole to the total unit-cell base area (when viewed from the bottom in Figure 7). This ratio, which quantifies the level of internal boundary scattering for a given membrane thickness, decreases as the unit-cell in-plane size is increased. We observe a noticeable increase in k_{NPX}/k_{Memb} between $b/a = 15$ CC ($c/a = 10$ CC) and $b/a = 18$ CC ($c/a = 12$ CC). These results show that an NPM with a high V_r volume fraction has more favorable performance characteristics with upscaling compared to a corresponding NPC with the same membrane thickness.

5. Summary and Future Directions for NPMs and NPCs

5.1. Summary

We have provided a literature and technical review of two emerging material concepts in nanoscale heat transfer with promising potential to serve as high-performance thermoelectric materials. Nanophononic metamaterials enable locally resonant motion to mix in with conventional phonon transport mechanisms leading to thermal conductivity reduction. Nanophononic crystals utilize periodicity to enable wave interferences that along with moderate boundary scattering from the periodic features also causes thermal conductivity reduction. Both NPMs and NPCs are nanostructured and typically formed from common semiconductors. Silicon in particular serves as an excellent constituent material owing to its relatively broad phonon mean-free-path distribution at room temperature and its low cost, favorable mechanical properties, and well-developed fabrication technology.

Both NPMs and NPCs are inspired by their larger-scale counterparts in the field of phononic crystals and acoustic/elastic metamaterials, respectively, where applications reside mostly within the hertz-to-megahertz operational range and typically revolve around a single frequency or a narrow band of frequencies. Phononic crystals have attracted interest mainly because of their bandgaps; and acoustic/elastic metamaterials are usually utilized for their unique effective properties in the subwavelength regime. In contrast, at the nanoscale the physics is profoundly different and the focus is not limited to bandgaps and subwavelength properties. Nanoscale thermal transport is a highly nonlinear, broadband process that extends well into the terahertz frequency regime. Focusing on NPMs, we outlined the three key mechanisms that arise due to the local resonances and that give this emerging nanostructured material paradigm its advantageous character: group velocity reductions, mode localizations, and lifetime reductions near the phonon-vibron coupling regions in the band structure and possibly also due to changes in the boundary scattering environment. All three mechanisms in principle take place across the entire spectrum, leading to an unprecedented opportunity for extreme thermal conductivity reduction.

One NPM configuration that is particularly suited for thermoelectric energy conversion is a thin suspended membrane with nanopillars or nanowalls extending from one or both surfaces. Using MD simulations, a silicon membrane-based NPM has been shown to yield up to two-orders-of-magnitude reduction in the in-plane lattice thermal conductivity without

© 2019 WILEY-VCH Verlag GmbH & Co. KGaA, Weinheim

any use of scatterers in the main body of the membrane. We have investigated the effects of varying the nanopillar geometry or the unit-cell lateral dimensions on the thermal conductivity. The results show superior performance for NPMs compared to NPCs in the form of same-thickness membranes with nanoholes. While NPCs may be designed to exhibit significantly low thermal conductivities, this may only be realized by having large and closely packed nanoholes and thus a very small minimum feature size within the membrane; for example, an NPC with 79% nanoholes area coverage exhibits $k_{NPC}/k_{Memb} = 1.5\%$. An NPM with tall nanopillars, on the other hand, may be designed to possess even lower thermal conductivity yet without sacrificing the minimum feature size within the membrane portion (since no nanoholes or nanoinclusions are needed); in the corresponding example, an NPM with 79% nanopillar coverage is shown to exhibit $k_{NPM}/k_{Memb} = 0.9\%$. Most important, since this NPM setup does not need nanoholes (or any other form of inclusions), the base membrane is left free from any constraints to strong generation and transport of electrons—thus providing ideal conditions for increasing the thermoelectric figure-of-merit ZT by design. This is a key advantage of NPMs not only over NPCs, but also over the use of scattering inclusions in general as a means to increasing thermoelectric performance. NPMs with tall nanopillars have also been shown by our simulations to experience no deterioration with increase in size (within the realm of $L \leq \Lambda$; see Figure 1), in contrast to the corresponding NPCs.

5.2. Looking Forward

The past two decades have witnessed active research into the transport characteristics and performance potential of NPCs and these efforts are carrying on into the future. For NPMs, it is now five years since their discovery and the curiosity over their underlying physics and potential impact on thermoelectricity continues to grow.

Future research on NPMs, and NPCs, will necessarily be on providing a rich body of experimental research and on further exploring the effects of upscaling. Upscaling is critical because of the practicality of device design, fabrication, and function. Considering NPMs, we note that a monotonic improvement in performance will take effect with increasing nanoresonator (e.g., nanopillar or nanowall) size as long as the characteristic length scales of the unit cell as a whole are considerably within the span of the phonon MFP distribution. As the unit-cell feature sizes start approaching the far end of the MFP distribution, phonon–phonon scattering mechanisms will dominate and the impact of the three resonance-based effects that reduce the thermal conductivity will gradually diminish. How far can we go in upscaling before this limit becomes practically detrimental, at different temperatures, remains an open question. As more understanding develops on the upscaling limitations, as well as counter effects of other scattering mechanisms in general, progress will naturally arise in NPM-based device design, implementation, characterization, and optimization for industrial competitiveness.

Future research may also consider a hybrid between an NPC with nanoholes and an NPM with nanopillars, that is, a nanoscale version of the trampoline metamaterial proposed earlier for acoustic and elastic waves.[120] This way, additional Bragg scattering from the nanoholes and relatively lower resonance frequencies from the more compliant NPM base structure may be realized. As long as there is enough spacing between the nanoholes not to impede the electron transport, it is conceivable that this mixed nanohole-nanopillar configuration would harness more thermoelectric energy conversion compared to having only nanopillars. Explicit study of the electrical properties of both NPCs and NPMs is also an area that awaits in-depth investigations.

Finally, there are promising future opportunities in the utilization of NPMs, and NPCs, for other applications beyond thermal conductivity reduction and thermoelectrics. These two nanosystems are shaping up a new era in nanoscale science and technology—an era of nanophononics.

Appendix

Table A1. Values of thermal conductivity predictions plotted in Figure 10.

	k_{NPX}/k_{Memb}			
c/a [CC]	2	4	6	8
NPC	0.583 ± 0.106	0.311 ± 0.054	0.213 ± 0.035	0.166 ± 0.026
NPM_1	0.690 ± 0.119	0.635 ± 0.096	0.608 ± 0.092	0.440 ± 0.067
NPM_3	0.825 ± 0.136	0.641 ± 0.135	0.447 ± 0.074	0.343 ± 0.056
NPM_{60}	–	0.087 ± 0.016	$0.059 \pm \nu 0.010$	$0.045 \pm \nu 0.007$
	k_{NPX}/k_{Memb}			
c/a[CC]	10	12	14	16
NPC	0.122 ± 0.020	0.079 ± 0.014	0.044 ± 0.008	0.015 ± 0.003
NPM_1	0.3760 ± 0.065	0.336 ± 0.063	0.316 ± 0.055	0.186 ± 0.033
NPM_3	0.288 ± 0.048	0.185 ± 0.036	0.159 ± 0.031	0.118 ± 0.021
NPM_{60}	0.027 ± 0.005	0.020 ± 0.004	0.011 ± 0.002	0.009 ± 0.002

Table A2. Values of thermal conductivity predictions plotted in Figure 11.

	k_{NPX}/k_{Memb}		
b/a[CC]	4	6	8
NPC	0.011 ± 0.002	0.019 ± 0.003	0.032 ± 0.005
NPM_1	0.292 ± 0.074	0.404 ± 0.071	0.344 ± 0.063
NPM_3	0.184 ± 0.036	0.210 ± 0.037	0.237 ± 0.039
NPM_{60}	0.024 ± 0.007	0.021 ± 0.004	0.017 ± 0.003
	k_{NPX}/k_{Memb}		
b/a[CC]	10	12	
NPC	0.035 ± 0.006	0.100 ± 0.016	
NPM_1	0.429 ± 0.084	0.363 ± 0.061	
NPM_3	0.205 ± 0.035	0.209 ± 0.034	
NPM_{60}	0.016 ± 0.002	0.022 ± 0.004	

© 2019 WILEY-VCH Verlag GmbH & Co. KGaA, Weinheim

Acknowledgements

This research was partially supported by the Advanced Research Projects Agency-Energy (ARPA-E) grant number DE-AR0001056. This work utilized the RMACC Summit supercomputer, which is supported by the National Science Foundation (awards ACI-1532235 and ACI-1532236), the University of Colorado Boulder, and Colorado State University. The Summit supercomputer is a joint effort of the University of Colorado Boulder and Colorado State University. This work also used the Extreme Science and Engineering Discovery Environment (XSEDE) through allocation DMR160173, which is supported by National Science Foundation grant number ACI-1548562.[121] Reference 24 was corrected on February 19, 2020 before initial online publication.

Conflict of Interest

The authors declare no conflict of interest.

Keywords

nanophononics, nanophononic crystals, nanophononic metamaterials, thermal transport, thermoelectric materials

Received: August 15, 2019
Revised: September 15, 2019
Published online: November 4, 2019

[1] N. W. Ashcroft, N. D. Mermin, *Solid State Physics*, Saunders College Publishing, Fort Worth, TX **1976**.
[2] B. L. Davis, M. I. Hussein, *Phys. Rev. Lett.* **2014**, *112*, 055505.
[3] M. I. Hussein, B. L. Davis, *US Patent 9,417,465*, **2016**.
[4] D. M. Rowe, *Thermoelectrics Handbook: Macro to Nano*, CRC Press, Boca Raton, FL **2005**.
[5] J. Tang, H.-T. Wang, D. H. Lee, M. Fardy, Z. Huo, T. P. Russell, P. Yang, *Nano Lett.* **2010**, *10*, 4279.
[6] J. K. Yu, S. Mitrovic, D. Tham, J. Varghese, J. R. Heath, *Nat. Nanotechnol.* **2010**, *5*, 718.
[7] K. Esfarjani, G. Chen, H. T. Stokes, *Phys. Rev. B* **2011**, *84*, 085204.
[8] G. Chen, *Int. J. Therm. Sci.* **2000**, *39*, 471.
[9] A. A. Balandin, *J. Nanosci. Nanotechnol.* **2005**, *5*, 1015.
[10] N. Li, J. Ren, L. Wang, G. Zhang, P. Hänggi, B. Li, *Rev. Mod. Phys.* **2012**, *84*, 1045.
[11] D. G. Cahill, P. V. Braun, G. Chen, D. R. Clarke, S. Fan, K. E. Goodson, P. Keblinski, W. P. King, G. D. Mahan, A. Majumdar, H. J. Maris, S. R. Phillpot, E. Pop, S. Li, *Appl. Phys. Rev.* **2014**, *1*, 011305.
[12] S. Volz, J. Ordonez-Miranda, A. Shchepetov, M. Prunnila, J. Ahopelto, T. Pezeril, G. Vaudel, V. Gusev, P. Ruello, E. M. Weig, M. Schubert, M. Hettich, M. Grossman, T. Dekorsy, F. Alzina, B. Graczykowski, E. Chavez-Angel, J. S. Reparaz, M. R. Wagner, C. M. S. Torres, S. Xiong, S. Neogi, D. Donadio, *Eur. Phys. J. B* **2016**, *89*, 15.
[13] G. P. Srivastava, *The Physics of Phonons*, Adam Hilger, Bristol, UK **1990**.
[14] S. Neogi, J. S. Reparaz, L. F. C. Pereira, B. Graczykowski, M. R. Wagner, M. Sledzinska, A. Shchepetov, M. Prunnila, J. Ahopelto, C. M. Sotomayor-Torres, D. Donadio, *ACS Nano* **2015**, *9*, 3820.
[15] M. I. Hussein, M. J. Leamy, M. Ruzzene, *Appl. Mech. Rev.* **2014**, *66*, 040802.
[16] A. S. Phani, J. Woodhouse, N. A. Fleck, *J. Acoust. Soc. Am.* **2006**, *119*, 1995.
[17] M. I. Hussein, G. M. Hulbert, *J. Sound Vib.* **2007**, *307*, 865.
[18] M. I. Hussein, M. J. Frazier, *J. Sound Vib.* **2013**, *332*, 4767.
[19] K. H. Matlack, A. Bauhofer, S. Sebastian Krödel, A. Palermo, C. Daraio, *J. Sound Vib.* **2016**, *307*, 8386.
[20] F. Cervera, L. Sanchis, J. V. Sánchez-Pérez, R. Mártnez-Sala, C. Rubio, F. Meseguer, C. López, D. Caballero, J. Sánchez-Dehesa, *Phys. Rev. Lett.* **2002**, *88*, 023902.
[21] S. X. Yang, J. H. Page, Z. Y. Liu, M. L. Cowan, C. T. Chan, P. Sheng, *Phys. Rev. Lett.* **2004**, *93*, 024301.
[22] M. I. Hussein, S. Biringen, O. R. Bilal, A. Kucala, *Proc. R. Soc. A* **2015**, *471*, 20140928.
[23] P. Wang, K. Bertoldi, *Phys. Rev. Lett.* **2015**, *115*, 104302.
[24] M. S. Garcia, V. Peri, R. Süsstrunk, O. R. Bilal, T. Larsen, L. G. Villanueva, S. D. Huber, *Nature* **2018**, *555*, 342.
[25] N. Swinteck, S. Matsuo, K. Runge, J. O. Vasseur, P. Lucas, P. A. Deymier, *J. Apl. Phys.* **2015**, *118*, 063103.
[26] G. Trainiti, M. Ruzzene, *New J. Phys.* **2016**, *18*, 083047.
[27] M. A. Attarzadeh, M. Nouh, *J. Sound Vib.* **2018**, *422*, 264.
[28] P. A. Deymier, Ed, *Acoustic Metamaterials and Phononic Crystals*, Springer, Heidelberg **2013**.
[29] V. Laude, *Phononic Crystals: Artifical Crystals for Sonic, Acoustic and Elastic Waves*, De Gruyter, Berlin **2015**.
[30] *Dynamics of Lattice Materials* (Eds: A. S. Phani, M. I. Hussein), Wiley, New York **2017**.
[31] M. V. Simkin, G. D. Mahan, *Phys. Rev. Lett.* **2000**, *84*, 927.
[32] A. N. Cleland, D. R. Schmidt, C. S. Yung, *Phys. Rev. B* **2001**, *64*, 172301.
[33] D. A. Broido, T. L. Reinecke, *Phys. Rev. B* **2004**, *70*, 081310(R).
[34] Y. Che, D. Li, J. Lukes, Z. Ni, M. Chen, *Phys. Rev. B* **2005**, *72*, 174302.
[35] A. J. H. McGaughey, M. I. Hussein, E. S. Landry, M. Kaviany, G. M. Hulbert, *Phys. Rev. B* **2006**, *74*, 104304.
[36] P. E. Hopkins, C. M. Reinke, M. F. Su, R. H. Olsson III, E. A. Shaner, Z. C. Leseman, J. R. Serrano, L. M. Phinney, I. El-Kady, *Nano Lett.* **2011**, *11*, 107.
[37] Y. P. He, D. Donadio, J. H. Lee, J. C. Grossman, G. Galli, *ACS Nano* **2011**, *5*, 1839.
[38] J. F. Robillard, K. Muralidharan, J. Bucay, P. A. Deymier, W. Beck, D. Barker, *Chin. J. Phys.* **2011**, *49*, 448.
[39] N. Zen, T. A. Puurtinen, T. J. Isotalo, S. Chaudhuri, I. J. Maasilta, *Nat. Commun.* **2014**, *5*, 3435.
[40] S. Alaie, D. F. Goettler, M. Su, Z. C. Leseman, C. M. Reinke, I. El-Kady, *Nat. Commun.* **2015**, *6*, 7228.
[41] J. N. Gillet, Y. Chalopin, S. Volz, *J. Heat Transfer* **2009**, *131*, 043206.
[42] B. L. Davis, M. I. Hussein, *AIP Adv.* **2011**, *1*, 041701.
[43] L. Yang, N. Yang, B. Li, *Nano Lett.* **2014**, *14*, 1734.
[44] In a phononic crystal, a band gap can only emerge when the wavelength is on the order of the unit-cell size or smaller. In general, the smaller the ratio of the wavelength to the unit-cell size, the harder it is to open band gaps. Since in macroscale phononic crystals the interest typically revolves around band gaps, unit cells are often designed such that the wavelength is roughly the same size as the periodicity. In nanoscale thermal transport, in contrast, this design constraint is no longer relevant because thermal conductivity reduction is achieved by flattening of the dispersion curves across the full spectrum without necessarily the presence of band gaps. The unit cell size, however, should necessarily be relatively small compared to the MFP distribution at the temperature of interest.
[45] A. Jain, Y.-J. Yu, A. J. H. McGaughey, *Phys. Rev. B* **2013**, *87*, 195301.
[46] M. R. Wagner, B. Graczykowski, J. Reparaz, A. El Sachat, M. Sledzinska, F. Alzina, C. M. Sotomayor Torres, *Nano Lett.* **2016**, *16*, 5661.

 © 2019 WILEY-VCH Verlag GmbH & Co. KGaA, Weinheim

[47] G. Chen, M. S. Dresselhaus, G. Dresselhaus, J. P. Fleurial, T. Caillat, *Int. Mater. Rev.* **2003**, *48*, 45.
[48] C. J. Vineis, A. Shakouri, A. Majumdar, M. G. Kanatzidis, *Adv. Mater.* **2010**, *22*, 3970.
[49] G. Chen, M. S. Dresselhaus, G. Dresselhaus, J.-P. Fleurial, T. Caillat, *Int. Mater. Rev.* **2013**, *48*, 45.
[50] D. G. Cahill, R. O. Pohl, *Phys. Rev. B* **1987**, *35*, 4067.
[51] A. Eucken, *Forsch. Ceram. Abstr.* **1932**, *11*, 576.
[52] A. Eucken, *Forsch. Ceram. Abstr.* **1933**, *12*, 231.
[53] Based on the classic Eucken model, $k_{Porous}/k_{Solid} = (1 = \phi)/(1 + \phi/2)$, the thermal conductivity of bulk silicon with $\phi = 35\%$ porosity is 42 W m^{-1} K^{-1}.[5]
[54] H. Honarvar, M. I. Hussein, *Phys. Rev. B* **2016**, *93*, 081412(R).
[55] H. Honarvar, L. Yang, M. I. Hussein, *Appl. Phys. Lett.* **2016**, *108*, 263101.
[56] H. Honarvar, M. I. Hussein, *Phys. Rev. B* **2018**, *97*, 195413.
[57] M. I. Hussein, H. Honarvar, *Handbook of Materials Modeling: Applications: Current and Emerging Materials* (Eds: W. Andreoni, S. Yip), Vol. 2, Springer, New York **2018**, pp. 1–21.
[58] J. B. Pendry, A. J. Holden, D. J. Robbins, W. J. Stewart, *IEEE Trans. Microwave Theory Tech.* **1999**, *47*, 2075.
[59] D. R. Smith, W. J. Padilla, D. C. Vier, S. C. Nemat-Nasser, S. Schultz, *Phys. Rev. Lett.* **2000**, *84*, 4184.
[60] Z. Y. Liu, X. X. Zhang, Y. W. Mao, Y. Y. Zhu, Z. Y. Yang, C. T. Chan, P. Sheng, *Science* **2000**, *289*, 1734.
[61] Y. Pennec, B. Djafari-Rouhani, H. Larabi, J. O. Vasseur, A.-C. Hladky-Hennion, *Phys. Rev. B* **2008**, *78*, 104105.
[62] T. T. Wu, Z. G. Huang, T. C. Tsai, T. C. Wu, *Appl. Phys. Lett.* **2008**, *93*, 111902.
[63] Z. Liu, C. T. Chan, P. Sheng, *Phys. Rev. B* **2002**, *65*, 165116.
[64] M. J. Frazier, M. I. Hussein, *C. R. Phys.* **2016**, *17*, 565.
[65] R. Hochbaum, A. I. Renkun Chen, R. D. Delgado, W. Liang, E. C. Garnett, M. Najarian, A. Majumdar, P. Yang, *Nature* **2008**, *451*, 163.
[66] A. I. Boukai, Y. Bunimovich, J. Tahir-Kheli, J.-K. Yu, W. A. Goddard III, J. R. Heath, *Nature* **2008**, *451*, 168.
[67] In a membrane-based NPM with nanopillars standing on the surface, the nanopillars may be viewed as nanowires. The thermal conductivity we examine in this system corresponds to the in-plane thermal transport along the membrane. This is in stark contrast to examining the thermal conductivity, or thermal transport, along the nanowires as was earlier done in the literature. In a membrane-based NPM, the nanopillars (or branching nanowires) do not represent a transport path; rather these are branching-out substructures that influence the character of the phonon transport along the base membrane from which the nanopillars are attached.
[68] K. Biswas, J. He, I. D. Blum, C.-I. Wu, T. P. Hogan, D. N. Seidman, V. P. Dravid, M. G. Kanatzidis, *Nature* **2012**, *489*, 414.
[69] A. A. Balandin, K. L. Wang, *Phys. Rev. B* **1998**, *58*, 1544.
[70] M. S. Dresselhaus, G. Chen, M. Y. Tang, R. G. Yang, H. Lee, D. Z. Wang, Z. F. Ren, J.-P. Fleurial, P. Gogna, *Adv. Mat.* **2007**, *19*, 1043.
[71] Z. Y. Wei, J. K. Yang, K. D. Bi, Y. F. Chen, *J. Appl. Phys.* **2015**, *118*, 155103.
[72] S. Xiong, K. Sääskilahti, Y. A. Kosevich, H. Han, D. Donadio, S. Volz, *Phys. Rev. Lett.* **2016**, *117*, 025503.
[73] D. Ma, A. Arora, S. Deng, G. Xie, J. Shiomi, N. Yang, *Mater. Today Phys.* **2019**, *8*, 56.
[74] D. Ma, H. Ding, H. Meng, L. Feng, Y. Wu, J. Shiomi, N. Yang, *Phys. Rev. B* **2016**, *94*, 165434.
[75] T. Zhu, K. Swaminathan-Gopalan, K. J. Cruse, K. Stephani, E. Ertekin, *Adv. Funct. Mater.* **2018**, *28*, 1706268.
[76] M. I. Hussein, *US Patent 10,283,689*, **2019**.
[77] S. Xiong, D. Selli, S. Neogi, D. Donadio, *Phys. Rev. B* **2017**, *95*, 180301(R).
[78] Y.-Y. Liu, Y.-J. Zeng, P.-Z. Jia, X.-W. Cao, X.-H. Jiang, K.-Q. Chen, *J. Phys.: Condens. Mater.* **2018**, *30*, 275701.
[79] A. Giri, P. E. Hopkins, *Phys. Rev. B* **2018**, *98*, 045421.
[80] D. Ma, X. Wan, N. Yang, *Phys. Rev. B* **2018**, *98*, 245420.
[81] A. Giri, P. E. Hopkins, *J. Appl. Phys.* **2019**, *125*, 205102.
[82] A. Iskandar, A. Gwiazda, Y. Huang, M. Kazan, A. Bruyant, M. Tabbal, G. Lerondel, *J. Appl. Phys.* **2016**, *120*, 095106.
[83] Y.-Y. Liu, W.-X. Zhou, L.-M. Tang, K.-Q. Chen, *Appl. Phys. Lett.* **2014**, *105*, 203111.
[84] Y.-Y. Liu, W.-X. Zhou, K.-Q. Chen, *Sci. Rep.* **2015**, *5*, 17525.
[85] X. Yang, D. Yu, B. Cao, A. C. To, *ACS Appl. Mater. Interfaces* **2017**, *9*, 29.
[86] X.-K. Chen, J. Liu, Z.-X. Xie, Y. Zhang, Y.-X. Deng, K.-Q. Chen, *Appl. Phys. Lett.* **2018**, *113*, 121906.
[87] Z.-X. Xie, J.-Z. Liu, X. Yu, H.-B. Wang, Y.-X. Deng, K.-M. Li, Y. Zhang, *J. Appl. Phys.* **2015**, *117*, 114308.
[88] R. Anufriev, R. Yanagisawa, M. Nomura, *Nanoscale* **2017**, *9*, 15083.
[89] R. Anufriev, M. Nomura, *Sci. Technol. Adv. Mater.* **2018**, *19*, 863.
[90] B. Li, K. T. Tan, J. Christensen, *Phys. Rev. B* **2017**, *95*, 144305.
[91] B. Li, K. T. Tan, J. Christensen, *J. Appl. Phys.* **2018**, *123*, 205105.
[92] B. T. Spann, J. C. Weber, M. D. Brubaker, A. C. Treglia, S. Berweger, L. Yang, H. Honarvar, M. I. Hussein, M. Lee, K. A. Bertness, *Nanowire Week 2017*, Lund, Sweden, June **2017**.
[93] R. Tsu, J. G. Hernandez, *Appl. Phys. Lett.* **1982**, *41*, 1016.
[94] S. Périchon, V. Lysenko, B. Remaki, D. Barbier, B. Champagnon, *J. Appl. Phys.* **1999**, *86*, 4700.
[95] J. S. Reparaz, E. Chavez-Angel, M. R. Wagner, B. Graczykowski, J. Gomis-Bresco, F. Alzina, C. M. Sotomayor Torres, *Rev. Sci. Instrum.* **2014**, *85*, 034901.
[96] J. Maire, R. Anufriev, T. Hori, J. Shiomi, S. Volz, M. Nomura, *Sci. Rep.* **2018**, *8*, 4452.
[97] D. A. Young, C. Thomsen, H. T. Grahn, H. J. Maris, J. Tauc, in *Phonon Scattering in Condensed Matter* (Eds: A. C. Anderson, J. P. Wolfe), Springer, Berlin **1986**, p. 49.
[98] A. Paddock, G. L. Eesley, *J. Appl. Phys.* **1986**, *60*, 285.
[99] D. G. Cahill, *Rev. Sci. Instrum.* **2004**, *75*, 5119.
[100] F. H. Stillinger, T. A. Weber, *Phys. Rev. B* **1985**, *31*, 5262.
[101] J. D. Gale, A. L. Rohl, *Mol. Simul.* **2003**, *29*, 291.
[102] J. A. Thomas, J. E. Turney, R. M. Iutzi, C. H. Amon, A. J. H. McGaughey, *Phys. Rev. B* **2010**, *81*, 081411.
[103] A. J. H. McGaughey, J. M. Larkin, *Annu. Rev. Heat Transfer* **2014**, *17*, 49.
[104] T. Wang, G. K. H. Madsen, A. Hartmaier, *Modell. Simul. Mater. Sci. Eng.* **2014**, *22*, 035011.
[105] J. M. Larkin, J. E. Turney, A. D. Massicotte, C. H. Amon, A. J. H. McGaughey, *J. Comput. Theor. Nanosci.* **2014**, *11*, 249.
[106] S. Plimpton, *J. Comput. Phys.* **1995**, *117*, 1.
[107] J. A. Appclbaum, G. A. Baraff, D. R. Hamann, *Phys. Rev. B* **1976**, *14*, 588.
[108] E. Helfand, *Phys. Rev.* **1960**, *119*, 1.
[109] R. Zwanzig, *Annu. Rev. Phys. Chem.* **1965**, *16*, 1798.
[110] A. J. C. Ladd, B. Moran, W. G. Hoover, *Phys. Rev. B* **1986**, *34*, 5058.
[111] S. G. Volz, G. Chen, *Phys. Rev. B* **2000**, *61*, 2651.
[112] P. K. Schelling, S. R. Phillpot, P. Keblinski, *Phys. Rev. B* **2002**, *65*, 144306.
[113] At $c/a = 2$ CC, the nanopillar width for NPM_{60} is too small for its height; this worsens the convergence of the thermal conductivity with time in the Green–Kubo calculations and as a result, we obtain relatively large error bars.
[114] C. J. Gomes, M. Madrid, J. V. Goicochea, C. H. Amon, *J. Heat Transfer* **2006**, *128*, 1114.
[115] P. Heino, *Eur. Phys. J. B* **2007**, *60*, 171.

 © 2019 WILEY-VCH Verlag GmbH & Co. KGaA, Weinheim

[116] J. E. Turney, A. J. H. McGaughey, C. H. Amon, *J. Appl. Phys.* **2010**, *107*, 024317.
[117] We should also note that these predictions are expressed relative to the uniform membrane thermal conductivity, which in itself often gives considerable variability in MD predictions.
[118] A. Biswas, I. S. Bayer, A. S. Biris, T. Wang, E. Dervishi, F. Faupel, *Adv. Colloid Interface Sci.* **2012**, *170*, 2.
[119] B. K. Teo, X. H. Sun, *Chem. Rev.* **2007**, *107*, 1454.
[120] O. R. Bilal, M. I. Hussein, *Appl. Phys. Lett.* **2013**, *103*, 111901.
[121] J. Towns, T. Cockerill, M. Dahan, I. Foster, K. Gaither, A. Grimshaw, V. Hazlewood, S. Lathrop, D. Lifka, G. D. Peterson, R. Roskies, J. R. Scott, N. Wilkens-Diehr, *Comput. Sci. Eng.* **2014**, *16*, 62.

© 2019 WILEY-VCH Verlag GmbH & Co. KGaA, Weinheim